Journal of Materials Chemistry C

Zero-dimensional Cs4EuX6 (X=Br, I) All-Inorganic Perovskite Single Crystals for Gamma-ray Spectroscopy

Journal:	*Journal of Materials Chemistry C*
Manuscript ID	TC-COM-03-2018-001458.R3
Article Type:	Communication
Date Submitted by the Author:	13-Jun-2018

Complete List of Authors:	Wu, Yuntao; University of Tennessee, Han, Dan; East China Normal University, Department of Physics; East China Normal University, Key Laboratory of Polar Materials and Devices, Ministry of Education, School of Information Science and Technology Chakumakos, Bryan; Oak Ridge National Laboratory, Shi, Hongliang; Beihang University Chen, Shiyou; Lawrence Berkeley National Laboratory, Materials Sicences Division,; East China Normal University, Key Laboratory of Polar Materials and Devices, Ministry of Education, School of Information Science and Technology Du, Mao Hua ; Oak Ridge National Laboratory, Greeley, Ian; University of Tennessee Loyd, Matthew; University of Tennessee Rutstrom, Daniel; University of Tennessee Stand, Luis; University of Tennessee Koschan, Merry; University of Tennessee, Knoxville Melcher, Charles L.; University of Tennessee,

Zero-dimensional Cs_4EuX_6 (X=Br, I) All-Inorganic Perovskite Single Crystals for Gamma-ray Spectroscopy

Yuntao Wu,[a,b,] Dan Han,[c,d,e] Bryan C. Chakoumakos,[f] Hongliang Shi,[g] Shiyou Chen,[c] Mao-Hua Du,[e,*] Ian Greeley,[a,b] Matthew Loyd,[a,b] Daniel J. Rutstrom,[a,b] Luis Stand,[a,h] Merry Koschan,[a] and Charles L. Melcher[a,b,h,i]*

[a] Scintillation Materials Research Center, University of Tennessee, Knoxville, TN 37996, USA
[b] Department of Materials Science and Engineering, University of Tennessee, Knoxville, TN 37996, USA
[c] Key Laboratory of Polar Materials and Devices (Ministry of Education), East China Normal University, Shanghai 200241, China
[d] Department of Physics, East China Normal University, Shanghai 200241, China
[e] Materials Science and Technology Division, Oak Ridge National Laboratory, Oak Ridge, TN 37831, USA
[f] Neutron Scattering Division, Oak Ridge National Laboratory, Oak Ridge, TN 37831
[g] Key Laboratory of Micro-Nano Measurement-Manipulation and Physics (Ministry of Education), Department of Physics, Beihang University, Beijing 100191, China
[h] Bredesen Center for Interdisciplinary Research and Graduate Education, University of Tennessee, Knoxville, TN 37996, USA
[i] Department of Nuclear Engineering, University of Tennessee, Knoxville, TN 37996, USA

*E-mail: ywu52@utk.edu, caswyt@hotmail.com (Y. Wu); Fax: +1 (865) 974-4998; Tel: +1 (865) 974-0254
mhdu@ornl.gov (M. Du); Fax: +1 (865) 576-4944; Tel: +1 (865) 576-6711.

Abstract: Organic-inorganic and all-inorganic halide perovskites have become leading candidates toward high-performance optoelectronic devices and radiation detectors. In this work, we report novel zero-dimensional Cs_4EuX_6 (X=Br, I) perovskite single crystals as self-activated scintillators with superior performance for gamma-ray spectroscopy. Both Cs_4EuBr_6 and Cs_4EuI_6 single crystals grown by the Bridgman method were determined to have the trigonal crystal structure with the $R\bar{3}c$ space group, and have a melting point of approximately 540 °C. Cs_4EuBr_6 and Cs_4EuI_6 exhibit blue emission under UV excitation and high light yields of 78,000 ± 4000 photons/MeV and 53,000 ± 3000 photons/MeV under ^{137}Cs gamma-ray irradiation, respectively. In particular, the former represents the best result achieved for self-activated scintillators thus far. Thermally stimulated luminescence studies and density functional theory calculations elucidate the correlation between halogen vacancies and long-lived emission (afterglow) at room temperature in Cs_4EuX_6 (X=Br, I) single crystals. Our findings not only demonstrate the high gamma-ray detection efficiency in Cs_4EuX_6 (X=Br, I), but will further promote the development of 0D metal halide-based novel luminescent and radiation detection materials.

Keywords: Perovskites, zero-dimensional, radiation detection, scintillators.

1. Introduction

Organic–inorganic hybrid perovskites, such as methylammonium lead trihalide ($MAPbI_3$), have emerged as excellent optoelectronic materials for solar cells,[1-6] photodetectors,[7] and light-emitting diodes [8], and also exhibit potential as semiconductors for X-ray [9-11] and γ-ray [12] direct-conversion detection. The all-inorganic cesium lead halide perovskites are also regarded as candidate materials toward high performance optoelectronic devices.[16-19] Furthermore, the $CsPbBr_3$ single crystals are considered to be excellent semiconductors for X-ray and γ-ray detection at room temperature; the detection efficiency was reported to be comparable to that of the state-of-art cadmium zinc telluride.[20] Replacing the organic cations by Cs^+ in detector materials not only improves the material stability [15] but also increases the effective atomic number and the density, which are desirable for the efficient absorption of ionizing radiation.

An alternative and currently more widely adopted method for radiation detection is through the use of scintillators, which emit photons under ionizing radiation. Recent studies have shown that zero-dimensional (0D) hybrid organic-inorganic halide perovskites, in which the metal-halide octahdra are separated from each other by large organic cations, exhibit excellent photoluminescence quantum efficiency [close to unity in $(C_4N_2H_{14}X)_4SnBr_6$] [21] due to the efficient optical emission by excitons, which are strongly localized at the spatially isolated metal-halide octahedra. In this work, by replacing the organic cations by heavier Cs^+ and by incorporating the more efficient photon emitter Eu^{2+}, we developed new 0D halide perovskites Cs_4EuX_6 (X=Br, I) as self-activated scintillators with superior performance for γ-ray spectroscopy applications. To our best knowledge, this is the first report of 0D-halide-perovskite-based scintillators. Remarkably, our Cs_4EuBr_6 single crystals have already achieved the highest light yield for self-activated scintillators thus far. Most existing scintillators are activated by extrinsic dopants, which are prone to the inhomogeneous dopant distribution in the bulk crystal. The self-activated Cs_4EuX_6 (X=Br, I) single crystals exhibit both efficient and homogeneous luminescence, which are highly desirable for radiation detection.

2. Experimental

2.1 Crystal growth

Anhydrous, high-purity (99.999%) beads of CsI and CsBr (SAFC Hitech), (99.99%) $EuBr_2$ (Sigma-Aldrich), and (99.995%) EuI_2 (APL Engineered Materials) were used as starting materials. The 12 mm diameter Cs_4EuBr_6 and 7 mm diameter Cs_4EuI_6 single crystals were grown by the vertical Bridgman method. The compositions were mixed according to the formula units. The mixtures were then loaded into quartz ampoules. The ampoules were evacuated to 10^{-6} mbar, heated to 250°C, and kept for 10 hours at this temperature to remove residual water and oxygen impurities.

After baking, the ampoules were sealed and transferred to the Bridgman growth furnace. They were passed through a temperature gradient of 25-35 °C/cm with a pulling rate of 1 mm/h. Finally, the furnace was cooled to room temperature at 10 °C/h.

2.2 Single-crystal X-ray study

Crystal fragments (~0.001 mm^3) were isolated from the slowly-grown boules and suspended in paratone oil, after which each was mounted on a plastic loop attached to the copper pin/goniometer. Single-crystal diffraction data were collected at 250K using a Rigaku XtaLAB PRO diffractometer with graphite monochromated Mo Kα radiation (λ = 0.71073 Å) equipped with a Dectris Pilatus 200 K detector and an Oxford N-HeliX cryocooler. Peak indexing and integration were done using the Rigaku Oxford Diffraction CrysAlisPro software.[22] An ampirical absorption correction was applied using the SCALE3 ABSPACK algorithm as implemented CrysAliPro. The SIR-2011 in WinGX and SHELXL-2013 software packages were used for data processing and structure solution and refinement.[23-24] Crystal structure projections were made with VESTA.[25] The crystal structure data and single-crystal X-ray diffraction refinement results for Cs_4EuBr_6 and Cs_4EuI_6 are shown in Table S1 (Supporting information). The fractional atomic coordinates and equivalent isotropic displacement parameters for Cs_4EuBr_6 and Cs_4EuI_6 are given in Table S2 and Table S3 (Supporting information), respectively.

2.3 Computational methods

All calculations were based on density functional theory (DFT) implemented in the VASP code.[26] The interaction between ions and electrons was described by the projector augmented wave method.[27] The kinetic energy cutoff for the plane-wave basis is 325 eV. Experimental lattice parameters of Cs_4EuX_6 (X = Br, I) were used while the atomic positions were fully relaxed until the residual forces were less than 0.02 eV/ Å. Hybrid PBE0 functional,[28] which includes 25% non-local Fock exchange, was used in all calculations. The inclusion of a fraction of Fock exchange significantly improves the calculations of the band gap energy, defects, dopants, and excitons in insulators.[29,30,31-34] The charge transition level $\varepsilon(q/q')$ for the halogen vacancy is determined by the Fermi level (ε_f), at which the formation energies of the vacancy with the charge states *q* and *q*' are equal to each other. $\varepsilon(q/q')$ can be calculated using

$$\varepsilon(q/q') = \frac{E_{D,q'} - E_{D,q}}{q - q'}, \quad (1)$$

where $E_{D,q}$ ($E_{D,q'}$) is the total energy of the supercell that contains the relaxed structure of the vacancy at the charge state q (q').

2.4 Differential scanning calorimeter (DSC) measurements

DSC measurements were carried out on a Labsys EVO instrument. Approximately 50 mg single crystals within an alumina crucible were heated and cooled at 5 K/min under a flow of ultra-high purity argon. Each sample was measured twice using the same heating and cooling profile each time. For a baseline subtraction to the heat flow, the sample crucible pan was run empty in identical conditions prior to measuring with the sample.

2.5 Hygroscopicity measurements

Moisture sorption profiles were recorded using a Dynamic Vapor Sorption technique with a DVS Intrinsic instrument by Particulate Systems. All samples have almost the same size. The measurements were carried out at 25 °C for 120 min at a relative humidity of 40%. The temperature and humidity selected here are to reproduce the actual operational conditions of radiation detectors.

2.6 Optical property measurements

Optical transmission spectra were acquired with a Varian Cary 5000 UV-VIS-IR spectrophotometer in the range between 300 and 800 nm range.

Photoluminescence emission (PL) and excitation (PLE) spectra were obtained with a HORIBA Jobin Yvon Fluorolog-3 spectrofluorometer. The excitation light went through an excitation monochromator with a 1 nm bandpass to ensure a narrow wavelength range of excitation light. Similarly, the emission monochromator was set at 1 nm bandpass to select emission light of a specific wavelength. In the case of emission and excitation spectra, a 450W continuous xenon lamp was used as the excitation source.

Photoluminescence decay was measured on the same spectrofluorometer using a time-correlated-single-photon counting module. HORIBA Jobin Yvon NanoLEDs (pulsed light-emitting diodes) were used as the excitation source. The duration of the light pulse was shorter than 2 ns and therefore was not deconvoluted from the much longer decay profiles.

2.7 Scintillation property measurements

Scintillation decay times were measured using a time-correlated single-photon counting setup under ^{137}Cs source excitation.[35]

Absolute light yield (LY) measurements were recorded by using a pulse processing chain consisting of a Hamamatsu R2059 photomultiplier tube (PMT) operated at -1500 V_{bias}, an Ortec 672 amplifier, a Canberra model 2005 pre-amp and a Tukan 8k multi-channel analyzer. Each sample was directly coupled to the PMT using mineral oil, and a PTFE-lined dome-shaped reflector with a 50 mm radius was used to maximize the collection of light. The photoelectron yields were estimated by using the single photoelectron peak method. Measurements of the samples were made with a 10 μs shaping time to provide light integration. Each sample was measured under irradiation with a 15 μCi ^{137}Cs source. The LY measurement for each sample was conducted ten times by repeating the mounts and measurements. The reproducibility of the LY measurements is ±5%.

The energy resolution was measured using a 5 cm diameter high quantum efficiency Hamamatsu R6231-100 PMT. This PMT was operated at -1.0 kV V_{bias}. Non-proportionality (nPR) measurements were also measured using this PMT. We used discrete ^{133}Ba (356 keV), ^{241}Am (59.5 keV), ^{57}Co (122 keV), ^{22}Na (511 keV), and ^{137}Cs (32 and 662 keV) γ-ray sources to excite the crystals at energies from 32 to 662 keV. The energy resolution (E.R.) was calculated as the full width at half maximum (FWHM) of the photopeak divided by the position of the photopeak maximum.

An X-ray tube operated at 35 kV and 0.1 mA was used as the excitation source for X-ray excited radioluminescence (RL) measurements. The RL was measured via in-line transmission mode in which the generated X-ray, sample, and monochromator are linearly aligned. For the afterglow measurements, the crystals were coupled to a Hamamatsu R2059 photomultiplier tube covered with Tetratex TX3104 PTFE membrane. The crystals were irradiated with x-rays at room temperature for 15 min, after which X-ray beam was cutoff within 1 s and the luminescence emitted from crystal was recorded as a function of time.

2.8 Thermoluminescence measurements

For each thermoluminescence (TL) measurement, a sample was mounted on the cold finger of the cryostat. The pressure was reduced to 20 mTorr and the sample was then heated to 550 K to ensure that all traps were empty in the temperature range of interest. The samples were cooled to 10 K and irradiated by an X-ray generator (X-ray Model; CMX003) at 35 kV and 0.1 mA for 15 min. Subsequently, the sample was heated to 550 K at a rate of 3 K/min; noise due to thermionic emissions precluded the acquisition of good quality data above this temperature. A Hamamatsu H3177 PMT optically coupled to the cryostat's light transport interface was used to measure the spectrally unresolved emission from the sample. The PMT current signal was transformed into a

voltage signal using standard NIM electronics. A National Instruments 6002-E data acquisition card was then used to digitize this voltage signal. Software developed in-house was used to correlate the sample temperature with the signal intensity.

3. Results and discussion

3.1 Crystal growth and thermal behaviours

Single crystal boules of 12 mm diameter Cs_4EuBr_6 and 7 mm diameter Cs_4EuI_6 are shown in Figure 1 (a) and (b). The as-grown Cs_4EuI_6 crystal has a cloudy layer on the surface. This phenomenon is usually caused by the volatilization of the precursor materials, which deposit onto the surface of the grown crystal upon cooling. This can result in the formation of defects caused by the deviation of the composition from stoichiometric because some are more volatile than others. This phenomenon was not observed for Cs_4EuBr_6. Thin slabs were cut from the cylindrical region adjacent to the cone and polished on both radial surfaces. The polished Cs_4EuI_6 slab is shown in Figure 1(c). Both Cs_4EuBr_6 and Cs_4EuI_6 thin slabs are transparent, crack-free, and without visible inclusions. To quantitatively evaluate the optical quality, optical transmission spectra of 1 mm thick Cs_4EuBr_6 and Cs_4EuI_6 slabs were acquired. As shown in Figure 1(d), the optical transmittance of Cs_4EuBr_6 is above 70% between 450 and 800 nm, which is 5-10% better than that of Cs_4EuI_6. The differential scanning calorimetry scans of as-grown Cs_4EuBr_6 and Cs_4EuI_6 samples are shown in Figure 1(e). Both compounds have singular melting (T_m) and crystallization (T_c) peaks. The Cs_4EuBr_6 sample has a melting point of 545 °C and a crystallization point of 525 °C, close to that of Cs_4EuI_6 (T_m=540 °C and T_c=527 °C). The moisture absorption rates of Cs_4EuBr_6 and Cs_4EuI_6 single crystals were measured by using the dynamic vapor sorption technique. Their DVS curves are plotted in Figure 1(f) as well as the one of a NaI standard sample. The moisture absorption rate of Cs_4EuI_6 is about 1.5 times higher than that of NaI, but the rate of Cs_4EuBr_6 is significantly lower. The weight change for Cs_4EuBr_6 is only 0.3 wt% after two hours of exposure to 40% humidity at 25 °C. The slight hygroscopicity of Cs_4EuBr_6 is a significant advantage for halide scintillators because it is much easier to handle and package for practical applications.

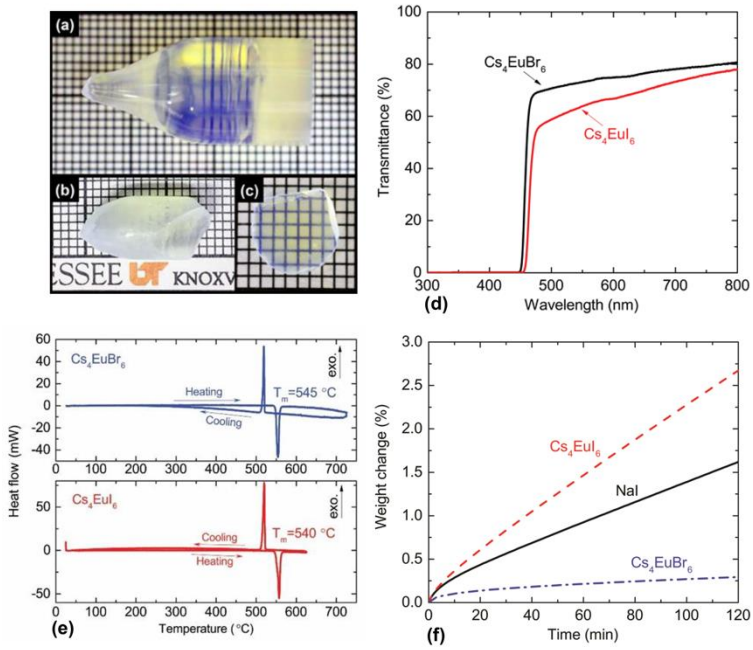

Figure 1. (a) A 12-mm diameter as-grown Cs_4EuBr_6 single crystal. (b) A 7-mm diameter as-grown Cs_4EuI_6 single crystal and (c) a 1-mm thick Cs_4EuI_6 slab. (d) Optical transmission spectra of 1 mm thick Cs_4EuBr_6 and Cs_4EuI_6 crystal slabs. (e) Differential scanning calorimeter curves of Cs_4EuBr_6 and Cs_4EuI_6 single crystals. (f) DVS curves of Cs_4EuBr_6 and Cs_4EuI_6 single crystals. The DVS curve of a NaI standard sample is also shown for comparison.

3.2 Crystal structure

The Cs_4EuBr_6 and Cs_4EuI_6 compounds both crystallize into the trigonal crystal system with the space group $R\bar{3}c$. A general formula of the halide perovskites is A_nBX_{2+n}, where A is a monovalent cation, B is a divalent metal, and X is a halogen anion. For Cs_4EuX_6 (X=Br, I), n equals 4 and the structure can be described as a zero-dimensional perovskite [36,37] because the $[EuX6]^{4-}$ octahedral are isolated dots. Crystal structure projections of Cs_4EuX_6 (X=Br, I) along the c-axis and a-axis are shown in Figure 2. These isolated and slightly distorted $[EuX_6]^{4-}$ (X=Br, I) octahedra are connected to Cs ions along the c-axis and form one-dimensional spiral chains of alternating $[EuX_6]^{4-}$ (X=Br, I) octahedral face-sharing with distorted $[CsI_6]^{5-}$ trigonal. The Cs atoms have two crystallographically independent sites (see Table S2 and Table S3). The refined crystal structure of Cs_4EuI_6 is consistent with that derived from X-ray powder diffraction study [38] and similar to Cs_4MI_6 (M=Ca, Sr) [39].

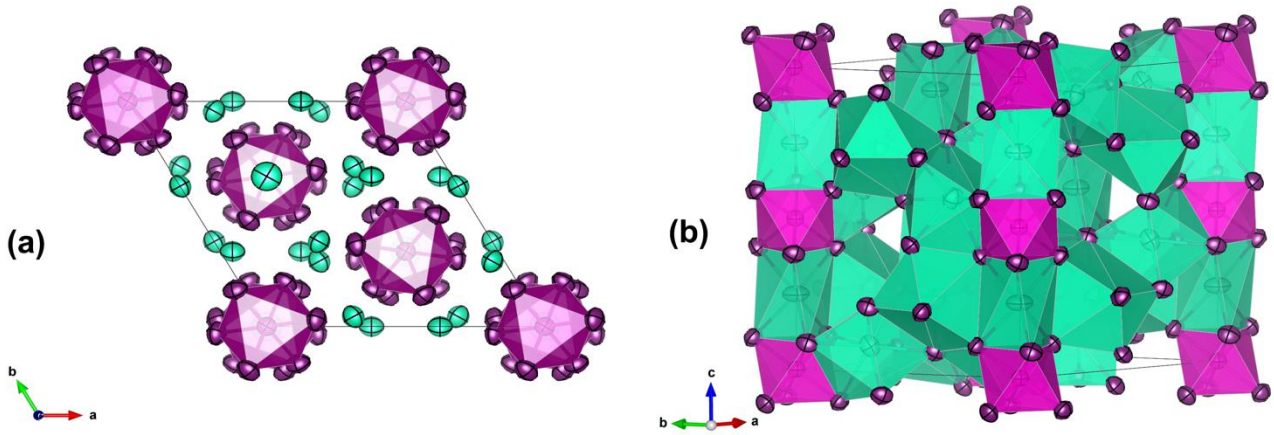

Figure 2. Crystal structure projections of Cs_4EuX_6 (X=Br, I) along the (a) c-axis and (b) a-axis, where the purple shaded polyhedral represent the tilted and isolated EuX_6^{4-} (X = Br, I) octahedra, and green and purple ellipsoids represent Cs and Br (or I) atoms, respectively.

3.3 Electronic Band structure

Figure 3 shows the band structures of Cs_4EuX_6 (X = Br, I). The band structures of both compounds exhibit Eu-4f-derived valence band maximum (VBM) and the Cs-6s-derived conduction band minimum (CBM). The fully occupied Eu-4f band in the spin-up channel is above the halogen p band; the flatness of this band is consistent with the strong localization of the Eu-4f orbitals. Although the Eu-5d states are above the CBM at the ground state as shown in Fig. 3, upon 4f-5d excitation, the Eu-5d level can be brought below the CBM by the strong Coulomb attraction between the electron on the 5d level and the hole on the 4f level. This is confirmed by the experimentally observed Eu^{2+} induced optical absorption, 2.74 eV for Cs_4EuBr_6 and 2.70 eV for Cs_4EuI_6 (see Figure 1(d)), which are significantly lower than the calculated fundamental band gaps of 3.9 eV and 4.2 eV, respectively. This indicates strong electron-hole binding in Eu^{2+} bound excitons. Between a bromide and an iodide with common cations, the band gap of the bromide is typically much larger than that of the iodide because the I-5p level is higher than the Br-4p level. However, the valence bands of Cs_4EuX_6 (X = Br, I) are both made up of Eu-4f states rather than the halogen p states; therefore, the calculated fundamental band gap and the measured optical absorption onset of Cs_4EuBr_6 are both close to those in Cs_4EuI_6.

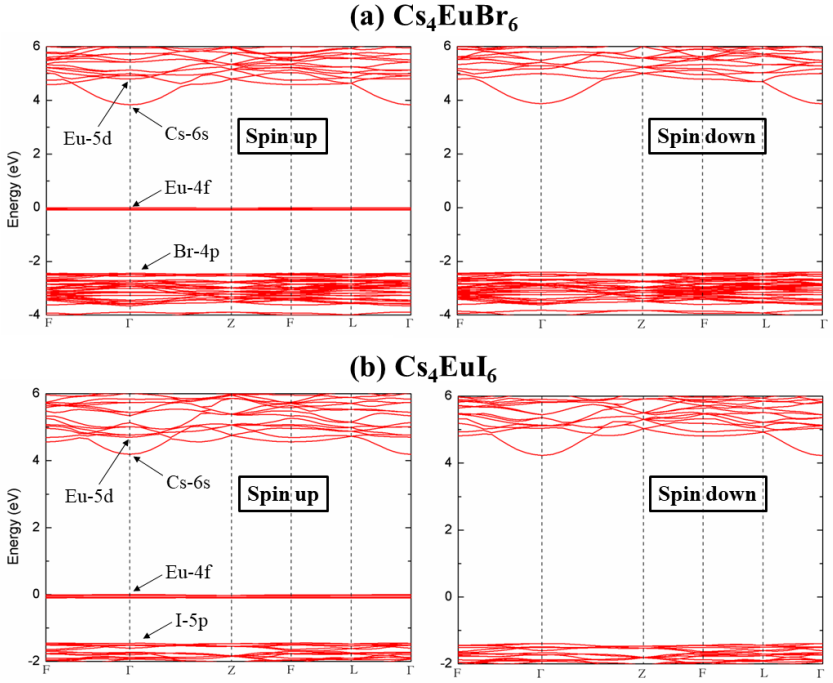

Figure 3. Band structures of (a) Cs_4EuBr_4 and (b) Cs_4EuI_6.

3.4 Optical and scintillation properties

The PLE and PL spectra of Cs_4EuBr_6 and Cs_4EuI_6 single crystals at room temperature are shown in Figure 4(a1) and (a2). For Cs_4EuI_6, the excitation spectrum monitored at an emission wavelength of 465 nm (Eu^{2+} $5d_1$-4f de-excitation) consists of several broad bands associated with the transitions from 4f ground state to the 5d excited states of Eu^{2+}. The Eu^{2+} $5d_1$-4f de-excitation of Cs_4EuBr_6 peaks at 455 nm. The Eu^{2+} 4f-$5d_1$ excitation band of Cs_4EuBr_6 is slightly redshifted in comparison to that of Cs_4EuI_6. The spectroscopic redshift is a combined effect of crystal field splitting (ε_{cfs}) and centroid shift (ε_c).[40] The ε_{cfs} is determined by the average distance to the coordinating ligands in the relaxed lattice structure around the Eu^{2+} provided the shape of the polyhedron is identical. The ε_{cfs} of Cs_4EuBr_6 should be higher than that of Cs_4EuI_6 because of the smaller effective ionic radii of Br^- compared to that of I^-. It leads to a redshift of the 4f-$5d_1$ transition of Cs_4EuBr_6 compared to that of Cs_4EuI_6. The spectroscopic polarizability α_{sp} is proportional to the centroid shift ε_c. For halide ions, the α_{sp} increases from F^-, Cl^-, Br^-, to I^-.[40] Thus, the ε_c of Cs_4EuI_6 is expected to be higher than that of Cs_4EuBr_6. Considering the opposite trend of ε_{cfs} and ε_c, the slight redshift observed in Cs_4EuBr_6 implies that crystal field splitting should be a more dominant factor than centroid shift.

For both Cs_4EuBr_6 and Cs_4EuI_6, the PL and RL emission can be well fitted by single Gaussian equation (see Figure 4(a2) and (b2)). It confirms the single Eu^{2+} crystallographic site in both

compounds derived from the crystal structure refinement. The red-shift and the broader full width at half maximum of the emission peak in the RL spectra compared to that of PL spectra can be ascribed to reabsorption that is related to the in-line transmission measurement geometry. Scintillation and PL decay profiles of Cs_4EuBr_6 and Cs_4EuI_6 are shown in Figure 4(a3) and (b3). The PL decay profiles of both Cs_4EuBr_6 and Cs_4EuI_6 are well fitted by two components, 0.75 μs (9.5%) and 2.92 μs (90.5%) for Cs_4EuBr_6 and 0.78 μs (23.5%) and 2.82 μs (76.5%) for Cs_4EuI_6. The scintillation decay time is expected to be longer than the lifetime of Eu^{2+} in both hosts, since the photoluminescence process occurred at activators is the final stage of the scintillation emission process. The Cs_4EuBr_6 has single scintillation decay component of 3.72 μs. The Cs_4EuI_6 has fast and slow decay components of 1.29 μs (17.7%) and 3.33 μs (82.3%), respectively.

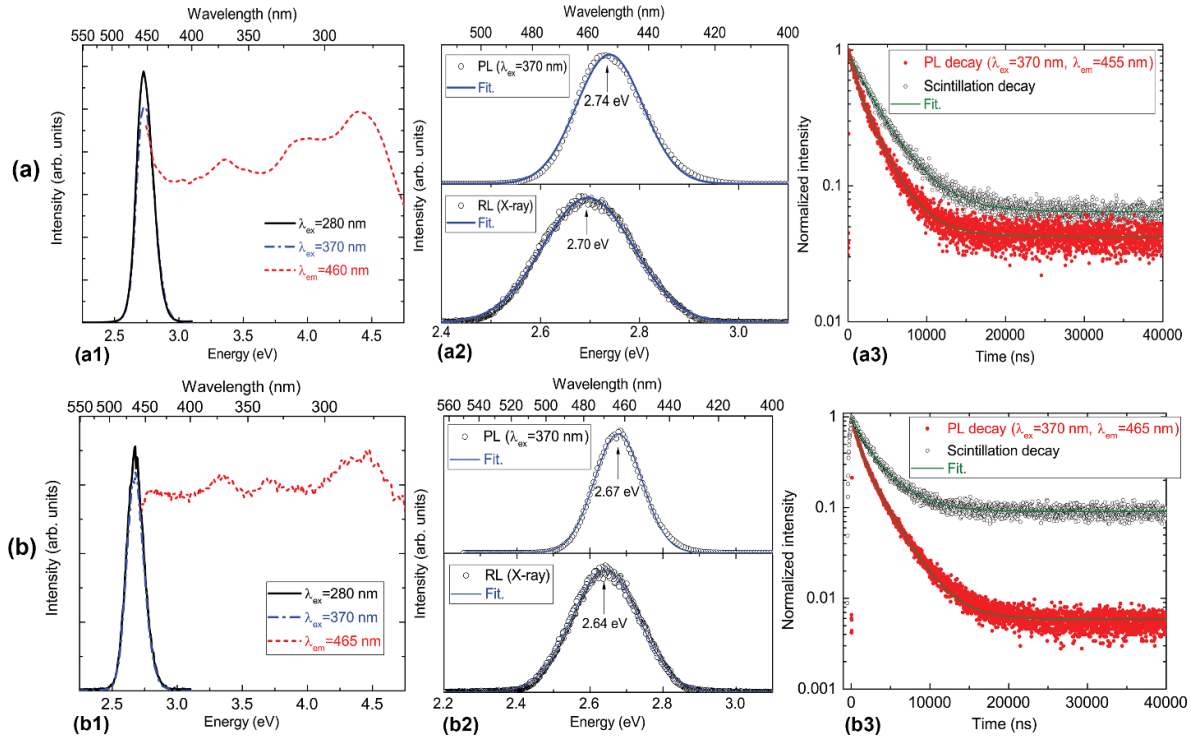

Figure 4. Photoluminescence emission and excitation spectra of (a1) Cs_4EuBr_6 and (b1) Cs_4EuI_6. The comparison between photoluminescence emission and X-ray induced radio-luminescence spectra: (a2) Cs_4EuBr_6 and (b2) Cs_4EuI_6. Photoluminescence and scintillation decay profiles of (a3) Cs_4EuBr_6 and (b3) Cs_4EuI_6.

Pulse height spectra of small-size Cs_4EuX_6 (X=Br, I) samples were acquired under ^{137}Cs irradiation with a calibrated Hamamatsu R2059 PMT (see Figure 5(a)). The spectrum of a BGO reference is also plotted for comparison. To evaluate absolute light yield for each sample, the emission-weighted quantum

efficiency (EWQE) of the photomultiplier tube (PMT) used is considered, namely 21.4% for Cs_4EuBr_6 and 21.2% for Cs_4EuI_6. A light yield of 78,000±4000 photons per MeV was estimated for Cs_4EuBr_6, about 30% higher than that of Cs_4EuI_6. It is worthwhile to mention that the light yield of Cs_4EuBr_6 is even higher than that of $CeBr_3$ (68,000 photons/MeV), the brightest self-activated scintillator ever reported.[41] Also, by comparing the light yield of 3D $CsEuI_3$ [42], 1D Cs_3EuI_5 [43], and the 0D Cs_4EuI_6 (see Figure 5(b)), it is clear that the scintillation yield significantly increases with the reduction of perovskite dimension. It suggests that the 0D structure with strongly localized excitons is beneficial for achieving high scintillation efficiency.

The energy resolution of small size Cs_4EuX_6 (X=Br, I) samples at 662 keV was measured with a Hamamatsu R6231-100 super bialkali PMT under ^{137}Cs gamma-ray source irradiation. The pulse height spectra and the Gaussian-fit curves of the full energy and escape peaks are both plotted in Figure 5(c). The energy resolution at 662 keV is 5.0±0.2% for Cs_4EuI_6 and 4.3±0.2% for Cs_4EuBr_6, respectively. For high light yield scintillators, the nPR is believed to be a dominant factor in determining the energy resolution.[44] The non-proportionality of Cs_4EuX_6 (X=Br, I) single crystals was measured by using different gamma-ray sources. The channel number of the full energy peak at each gamma-ray energy was determined, and the data points were then normalized with respect to the response at 662 keV. The ideal nPR response will be the same number of photons emitted per energy unit for any given gamma-ray energy. The measured nPR of Cs_4EuX_6 (X=Br, I) are shown in Figure 5(d) as well as the data of NaI:Tl for comparison. For both Cs_4EuX_6 (X=Br, I), the scintillation response above 356 keV is very proportional, but the proportionality becomes worse with decreasing gamma-ray energy, over 5% deviation at 32 keV. It has been suggested that the difference in nPR relies on the subtle but important distinction in electronic band structure.[45,46] Unlike SrI_2, a more proportional scintillator with 3% energy resolution at 662 keV, the bands above the CBM in both Cs_4EuX_6 (X=Br, I) are curved and dispersive. It implies a high linear quenching of hot electrons at deep traps due to their high group velocity, which can be responsible for the large deviation in proportionality. Because the scintillation response deviation of Cs_4EuI_6 is less than that of Cs_4EuBr_6 throughout the measured energies, its moderate energy resolution of 5% at 662 keV should be associated with its relatively low crystal quality. Therefore, it is expected that the energy resolution can be further improved via crystal growth optimization.

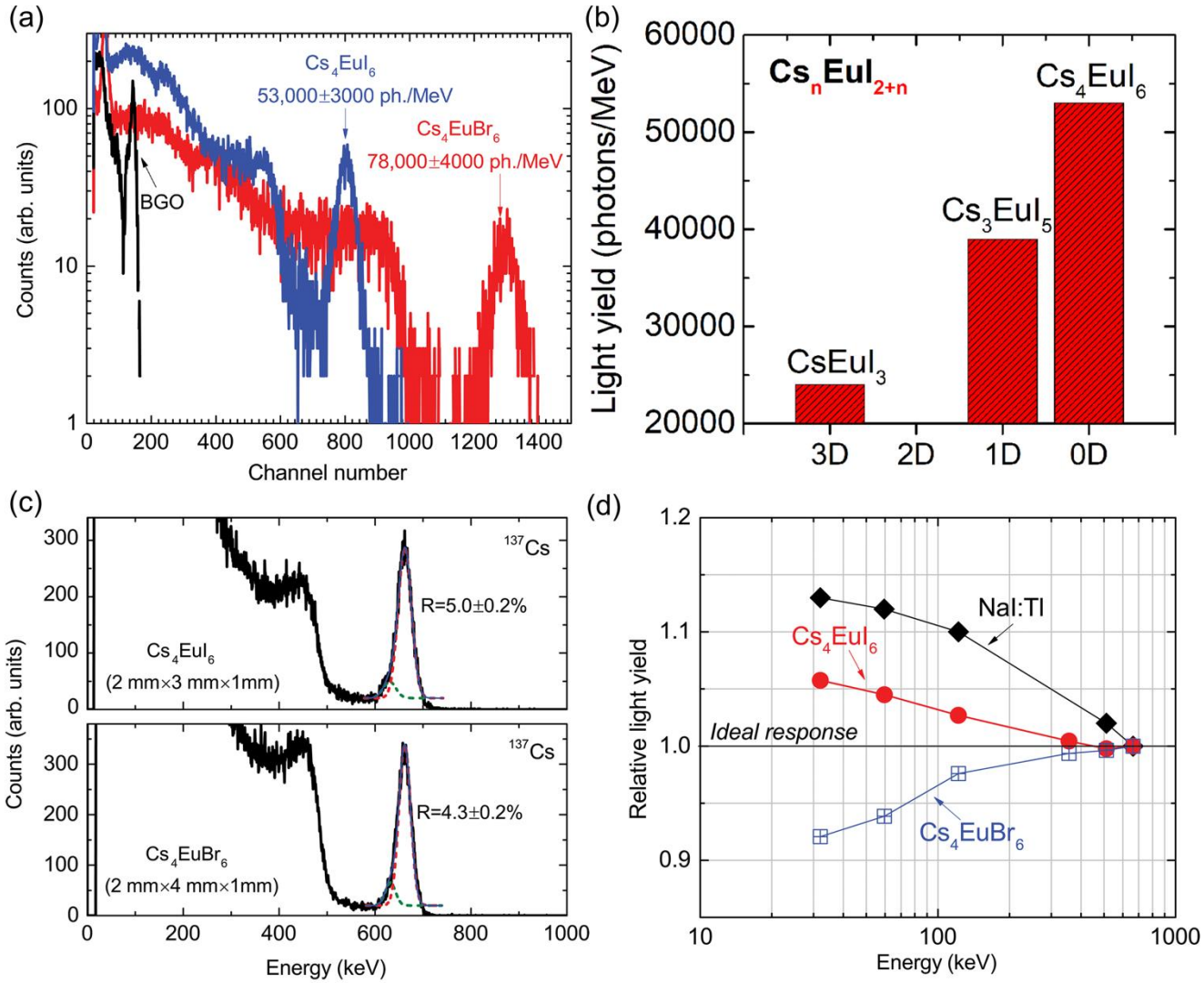

Figure 5. (a) ^{137}Cs pulse height spectra measured with Cs_4EuBr_6 and Cs_4EuI_6 single crystals coupled to a Hamamatsu R2059 PMT. (b) The correlation between perovskite dimension and scintillation light yield within Cs_nEuI_{2+n} (n=1, 3, and 4) material family. (c) ^{137}Cs pulse height spectra measured with Cs_4EuBr_6 and Cs_4EuI_6 single crystals coupled to a Hamamatsu R6231-100 PMT. (d) Light yield non-proportionality. The nPR curve of NaI:Tl is plotted as a reference.

3.5 Point defects

The X-ray induced afterglow profiles of Cs_4EuBr_6 and Cs_4EuI_6 single crystals are shown in Figure 6(a) along with that of a BGO reference. For Cs_4EuBr_6, the afterglow signal drops by over two orders of magnitude within the first ten seconds after the X-ray cut-off, and afterward decreases gradually. In comparison, the Cs_4EuI_6 crystal has much higher afterglow level throughout the entire measurement period. The residual signal of Cs_4EuI_6 decreases by less than two orders of magnitude in the first ten seconds, and

afterward its signal is over one order magnitude higher than that of Cs_4EuBr_6. The higher afterglow of Cs_4EuI_6 is probably attributed to its relatively lower light yield compared to that of Cs_4EuBr_6. To better understand the origin of afterglow, thermoluminescence measurements were performed on both samples. In Figure 6(b), the TL glow curve of Cs_4EuI_6 contains multiple peaks between 275 and 400 K, which should be associated with the room temperature afterglow observed. The afterglow-related TL peaks in Cs_4EuBr_6 are observed between 250 and 350 K. To quantitatively evaluate these TL peaks, the modified general-order kinetics expression describing TL intensity I as a function of temperature T is used to fit the glow curve:[47]

$$I(T) = sn_0 \exp\left(-\frac{E_t}{\kappa_B T}\right) \times \left\{\frac{(l-1)s}{\beta} \times T \times \exp\left(-\frac{E_t}{\kappa_B T}\right) \times \left[\left(\frac{\kappa_B T}{E_t}\right) - 2\left(\frac{\kappa_B T}{E_t}\right)^2 + 6\left(\frac{\kappa_B T}{E_t}\right)^3\right] + 1\right\}^{l/(1-l)} \quad (2)$$

where n_0 is the concentration of trapped charges at t=0, E_t the energy level of the trap, κ_B the Boltzmann constant, l the kinetic order, s the frequency factor, and β the heating rate (3 $Kmin^{-1}$ in this measurement). The fitting parameters agree well with the experimental data (see Figure 6b). On a basis of the trap parameters, the de-trapping time τ at the temperature T can be calculated as:[47]

$$\tau = s^{-1} \times e^{E/kT} \quad (3)$$

The temperature, trap depth, frequency, and detrapping time at RT are all listed in Table 1. For both compounds, the depths of these deep electron traps are between 0.69 and 1.07 eV and the corresponding de-trapping times are on the order of seconds, minutes, or even hours. For single crystal halides, the halogen vacancies with different charge states are able to form deep electron traps.[48-50] For example, for binary halides, such as $LaBr_3:Ce^{3+}$, the energetic depth of the Br vacancy with one captured electron is 0.94 eV below the conduction band minimum (CBM).[48,49] For $SrI_2:Eu^{2+}$, the trap depths for I vacancy with one electron and two electrons are 1.56 eV and 1.17 eV below the CBM, respectively.[50] For ternary halides, such as $KCaI_3:Eu^{2+}$, The trap depth of iodide vacancies is about 1 eV below the CBM.[51] Our calculations show that the halogen vacancies in Cs_4EuX_4 (X = Br, I) are both deep amphoteric defects, which can trap electrons. The calculated halogen vacancy induced defect levels are shown in Figure 6 (c) and (d). They are in good agreement with the experimentally evaluated depths of the afterglow-related deep electron traps. Thus, for Cs_4EuBr_6 and Cs_4EuI_6, it is believed that some of the radiation-generated holes and electrons are trapped by Eu ions and halogen vacancies which are not adjacent to each other. Then, the slow thermal excitation of the electrons deeply trapped at halogen vacancies back to the conduction band causes the

afterglow. The stronger afterglow in Cs_4EuI_6 than in Cs_4EuI_6 is likely because V_I is more abundant in Cs_4EuI_6 than V_{Br} in Cs_4EuBr_6.

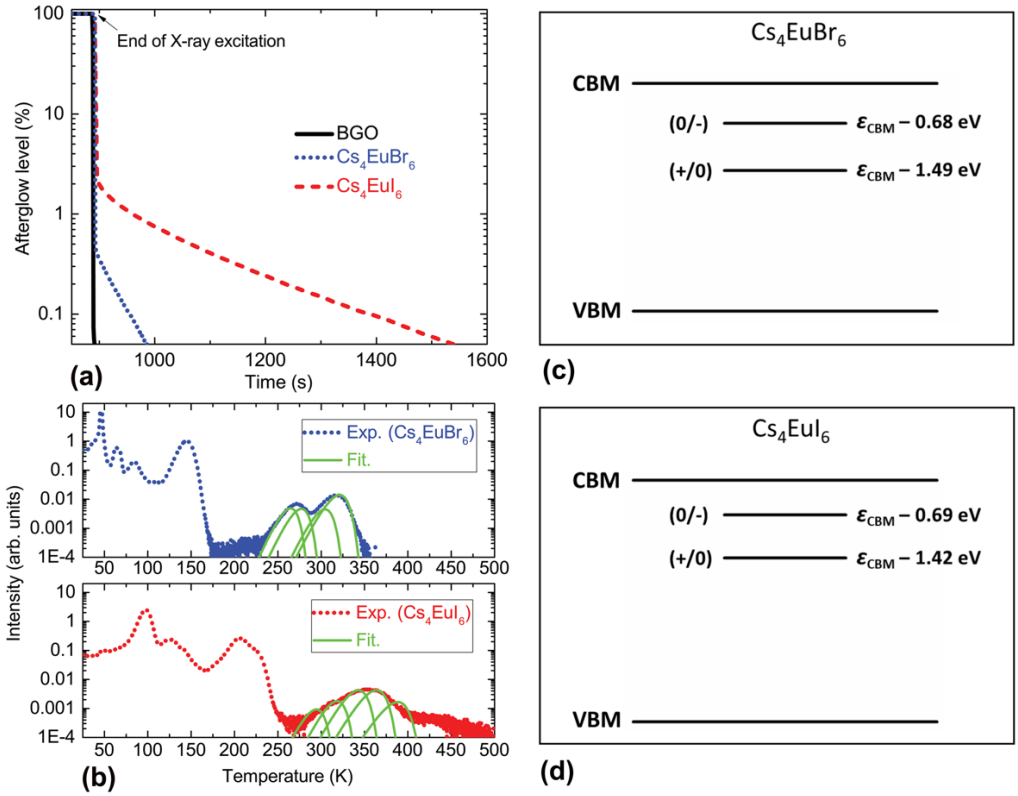

Figure 6. (a) X-ray induced afterglow profiles and (b) thermoluminescence glow curves of Cs_4EuBr_6 and Cs_4EuI_6 single crystals. The fitted TL peaks are potted in green. Calculated defect levels of (c) V_{Br} in Cs_4EuBr_6 and (d) V_I in Cs_4EuI_6.

Table 1. Fitted TL kinetic parameters of Cs_4EuBr_6 and Cs_4EuI_6.

Composition	T_{max} /(K)	E_{trap} /(eV)	s /(s^{-1})	τ_{RT} /(s)
Cs_4EuBr_6	264	0.69	2.5×10^{11}	2
	278	0.73	2.5×10^{11}	6
	305	0.85	2×10^{12}	101
	322	0.88	1×10^{12}	646
Cs_4EuI_6	295	0.77	2.5×10^{11}	37
	319	0.90	2×10^{12}	480
	343	0.94	1×10^{12}	6.9×10^{3}
	364	1.00	1×10^{12}	6.7×10^{4}
	389	1.07	1×10^{12}	1.0×10^{6}

4. Conclusions

High quality Cs_4EuBr_6 and Cs_4EuI_6 single crystals were grown by the Bridgman method. Both compounds have a trigonal crystal structure with R$\bar{3}$c space group. The melting points and crystallization points were determined to be 545 and 525°C for Cs_4EuBr_6 and 540 and 527°C for Cs_4EuI_6. The band structures of both compounds exhibit Eu-4f-derived valence band maximum and Cs-6s-derived conduction band minimum. The Cs_4EuBr_6 and Cs_4EuI_6 single crystals achieve gamma-ray energy resolutions of 4.3% and 5.0% at 662 keV, respectively, and high light yields of 78,000 ± 4000 and 53,000 ± 3000 photons/MeV. Remarkably, the light yield of Cs_4EuBr_6 is the highest among self-activated scintillators. The observed afterglow in both compounds are attributed to the halogen-vacancy- related deep electron traps based on thermoluminescence measurements and theoretical calculations. The zero-dimensional all-inorganic perovskites reported here are self-activated blue emitters with slight hygroscopicity, high radiation detection efficiency and scalable synthesis, which opens a new avenue for the application of perovskite materials as radiation detection and luminescent materials.

Conflicts of interest

There are no conflicts to declare.

Acknowledgements

This work was supported by Siemens Medical Solutions. The work at ORNL were supported by the U. S. Department of Energy, Office of Science, Basic Energy Sciences, Materials Sciences and Engineering Division. H. Shi was supported by the National Natural Science Foundation of China (NSFC) under Grants No.11604007 and the start-up funding at Beihang University. D. Han and S. Chen were supported by NSFC under grant Nos. 61574059 and 61722402, Shu-Guang program (15SG20) and CC of ECNU.

References

1 M. Liu, M. B. Johnston, and H. J. Snaith, *Nature* 2013, **501**, 395.

2 Q. Dong, Y. Fang, Y. Shao, P. Mulligan, J. Qiu, L. Cao, J. Huang, *Science* 2015, **347**, 967.

3 N. J. Jeon, J. H. Noh, W. S. Yang, Y. C. Kim, S. Ryu, J. Seo, and S. Seok, *Nature* 2015, **517**, 476.

4 Q. Lin, A. Armin, R. C. R. Nagiri, P. Burn, and P. Meredith, *Nature Photonics* 2015, **9**, 106-112.

5 D. Shi, V. Adinolfi, R. Comin, M. Yuan, E. Alarousu, A. Buin, Y. Chen, S. Hoogland, A. Rothenberger, K. Katsiev, Y. Losovyj, X. Zhang, P. A. Dowben, O. F. Mohammed, E. H. Sargent, and O. M. Bakr, *Science* 2015, **347**, 519.

6 H. Zhou, Q. Chen, G. Li, S. Luo, T. Song, H. Duan, Z. Hong, J. You, Y. Liu, and Y. Yang, *Science* 2014, **345**, 542.

7 Y. Fang, Q. Dong, Y. Shao, Y. Yuan, and J. Huang, *Nature Photonics* 2015, **9**, 679.

8 Q. Chen, N. D. Marco, Y. Yang, T. Song, C. Chen, H. Zhao, Z. Hong, H. Zhou, and Y. Yang, *Nano Today* 2015, **10**, 355.

9 H. Wei, Y. Fang, P. Mulligan, W. Chuirazzi, H. Fang, C. Wang, B. R. Ecker, Y. Gao, M. A. Loi, L. Cao, and J. Huang, *Nature Photonics* 2016, **10**, 333.

10 W. Wei, Y. Zhang, Q. Xu, H. Wei, Y. Fang, Q. Wang, Y. Deng, T. Li, A. Gruverman, L. Cao, and J. Huang, *Nature Photonics* 2017, **11**, 315.

11 Y. C. Kim, K. H. Kim, D. Son, D. Jeong, J. Seo, Y. Choi, I. T. Han, S. Y. Lee, and N. Park, *Nature* 2017, **550**, 87.

12 H. Wei, D. DeSantis, W. Wei, Y. Deng, D. Guo, T. J. Savenije, L. Cao, and J. Huang, *Nature Mater.* 2017, **16**, 826,

13 S. Yakunin, M. Sytnyk, D. Kriegner, S. Shrestha, M. Richter, G. J. Matt, H. Azimi, C. J. Brabec, J. Stangl, M. V. Kovalenko, and W. Heiss, *Nature Photonics* 2015, **9**, 444.

14 B. Conings, J. Drijkoningen, N. Gauquelin, A. Babayigit, J. D'Haen, L. D'Olieslaeger, A. Ethirajan, J. Verbeeck, J. Manca, E. Mosconi, F. D. Angelis, and H. Boyen, *Adv. Energy Mater.* 2015, **5**, 1500477.

15 M. Kulbak, S. Gupta, N. Kedem, I. Levine, T. Bendikov, G. Hodes, and D. Cahen, *J. Phys. Chem. Lett.* 2016, **7**, 167.

16 J. Song, J. Li, X. Li, L. Xu, Y. Dong, H. Zeng, *Adv. Mater.* 2015, **27**, 7162.

17 N. Yantara, S. Bhaumik, F. Yan, D. Sabba, H. A. Dewi, N. Mathews, P. P. Boix, H. V. Demir, and S. Mhaisalkar, *J. Phys. Chem. Lett.* 2015, **6**, 4360.

18 X. Li, Y, Wu, S. Zhang, B. Cai, Y. Gu, J. Song, H. Zeng, *Adv. Funct. Mater.* 2016, **26**, 2435.

19 H. Lu, W. Tian, F. Cao, Y. Ma, B. Gu, L. Li, *Adv. Funct. Mater.* 2016, **26**, 1296−1302.

20 C. C. Stoumpos, C. D. Malliakas, J. A. Peters, Z. Liu, M. Sebastian, J. Im, T. C. Chasapis, A. C. Wibowo, D. Y. Chung, A. J. Freeman, B. W. Wessels, and M. G. Kanatzidis, *Cryst. Growth Des.* 2013, **13**, 2722.

21 C. Zhou, H. Lin, Y. Tian, Z. Yuan, R. J. Clark, B. Chen, B. van de Burgt, J. C. Wang, Y. Zhou, K. Hanson, Q. Meisner, J. Neu, T. Besara, T. Siegrist, E. Lambers, P. I. Djurovich, B. Ma, *Chem. Sci.* 2018, **9**, 586.

22 Rigaku, CrystalClear. Rigaku Corporation, Tokyo, Japan, 2005.

23 G. M. Sheldrick, *Acta Crystallogr.* 2008, **A64**, 112.

24 L. J. Farrugia, *J. Appl. Cryst.* 2012, **45**, 849.

25 K. Momma and F. Izumi, *J. Appl. Crystallogr.* 2008, **41**, 653.

26 G. Kresse and J. Furthmüller, *Computational Materials Science* 1996, **6**, 15.

27 G. Kresse and D. Joubert, *Physical Review B* 1999, **59**, 1758.

28 J. P. Perdew, M. Emzerhof and K. Burke, *Journal of Chemical Physics* 1996, **105**, 9982.

29 M.-H. Du and S. B. Zhang, *Physical Review B* 2009, **80**, 115217.

30 J. B. Varley, A. Janotti, C. Franchini and C. G. Van de Walle, *Physical Review B* 2012, **85**, 081109.

31 K. Biswas and M. H. Du, *Physical Review B* 2012, **86**, 014102.

32 M. H. Du, *Journal of Materials Chemistry C* 2014, **2**, 4784.

33 M. H. Du, *ECS J. Solid State Sci. Technol.* 2016, **5**, R3007.

34 C. Zhou, H. Lin, H. Shi, Y. Tian, C. Pak, M. Shatruk, Y. Zhou, P. Djurovich, M.-H. Du and B. Ma, *Angewandte Chemie International Edition*, 2018, **57**, 1021.

35 L. M. Bollinger and G. E. Thomas, *Review of Scientific Instruments* 1961, **32**, 1044.

36 B. Saparov and D. B. Mitzi, *Chem. Rev.* 2016, **116**, 4558.

37 H. Tsai, W. Nie, J.-C. Blancon, C. C. Stoumpos, R. Asadpour, B. Harutyunyan, A. J. Neukirch, R. Verduzco, J. J. Crochet, S. Tretiak, L. Pedesseau, J. Even, M. A. Alam, G. Gupta, J. Lou, P. M. Ajayan, M. J. Bedzyk, M. G. Kanatzidis, and A. D. Mohite, *Nature* 2016, **536**, 312.

38 L. Chen, M. Wang, and S. Wang, *J. Alloys Compounds* 1997, **256(1-2)**, 112.

39 L. Stand, M. Zhuravleva, B. Chakoiumakos, J. Johnson, M. Loyd, Y. Wu, M. Koschan, and C. L. Melcher, *J. Cryst. Growth* 2018, **486**, 162.

40 P. Dorenbos, *Phys. Rev. B* 2000, **62**, 15650.

41 K. S. Shah, J. Glodo, W. Higgins, E. V. D. van Loef, W. W. Moses, S. E. Derenzo, and M. J. Weber, *IEEE Trans. Nucl. Sci.* 2005, **52**, 3157.

42 K. Yang, M. Zhuravleva, and C. L. Melcher, *Phys. Status Solidi RRL* 2011, **5(1)**, 43.

43 K. Yang, M. Zhuravleva, and C. L. Melcher, *J. Cryst. Growth* 2011, **318(1)**, 833.

44 P. Dorenbos, *IEEE Trans Nucl. Sci.* 2010, **57**, 1162.

45 Q. Li, J. Q. Grim, K. B. Ucer, A. Burger, G. A. Bizarri, W. W. Moses, and R. T. Williams, *Phys. Status Solidi RRL* 2012, **6**, 346.

46 Q. Feng and K. Biswas, *J. Appl. Phys.* 2016, **120**, 213104.

47 Y. Wu, H. Shi, B. C. Chakoumakos, M. Zhuravleva, M. Du, and C. L. Melcher, *J. Mater. Chem. C.*, 2015, **3**, 11366.

48 D. Åberg, B. Sadigh, A. Schleife and P. Erhart, *Appl. Phys. Lett.* 2014, **104**, 211908.

49 P. Erhart, B. Sadigh, A. Schleife and D. Åberg, *Phys. Rev. B* 2015, **91**, 165206.

50 Q. Li, R. T. Williams and D. Åberg, *Phys. Status Solidi B* 2013, **250**, 233.

51 Y. Wu, Q. Li, S. Jones, C. Dun, S. Hu, M. Zhuravleva, A. C. Lindsey, L. Stand, M. Loyd, M. Koschan, J. Auxier II, H. L. Hall, and C. L. Melcher, *Phys. Rev. Appl.* 2017, **8**, 034011.

A table of contents entry

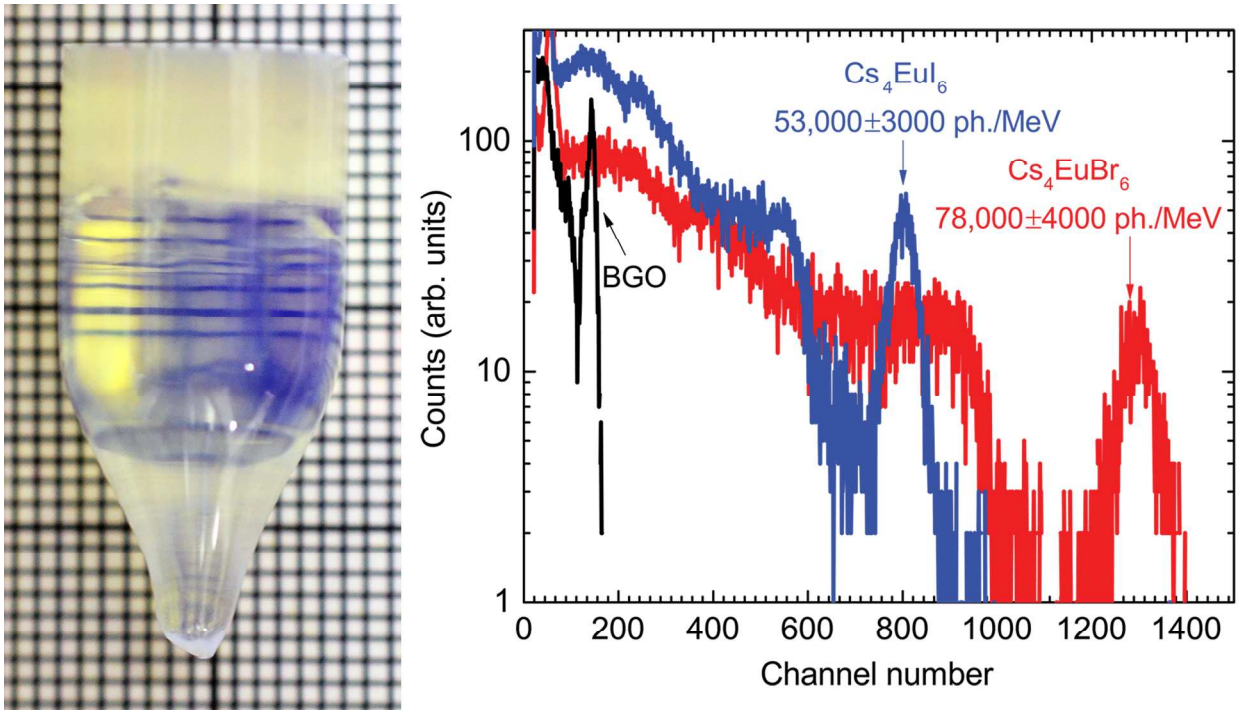

The zero-dimensional all-inorganic perovskites are self-activated blue emitters with slight hygroscopicity, scalable synthesis, and high radiation detection efficiency.